HHS Public Access

Author manuscript

Integr Biol (Camb). Author manuscript; available in PMC 2015 May 12.

Published in final edited form as:

Integr Biol (Camb). 2013 January ; 5(1): 74–86. doi:10.1039/c2ib20174g.

Clinically-translated silica nanoparticles as dual-modality cancer-targeted probes for image-guided surgery and interventions

Michelle S. Bradbury[a], **Evan Phillips**[a], **Pablo H. Montero**[b], **Sarah M. Cheal**[a], **Hilda Stambuk**[a], **Jeremy C. Durack**[a], **Constantinos T. Sofocleous**[a], **Richard J. C. Meester**[c], **Ulrich Wiesner**[d,†], and **Snehal Patel**[b,†]

Michelle S. Bradbury: bradburm@mskcc.org

[a]Department of Radiology, Sloan Kettering Institute for Cancer Research, 1275 York Ave., Z-2001, New York, NY 10065, USA. Fax: +1 (646)-888-3059; Tel: +1 (646)-888-3373

[b]Department of Surgery, Sloan Kettering Institute for Cancer Research, New York, NY 10065, USA

[c]Quest Medical Imaging B.V., Middenmeer, The Netherlands NL-1775PW

[d]Department of Materials Science & Engineering, 330 Bard Hall, Cornell University, Ithaca, NY 14853, USA

Abstract

Early diagnosis and treatment of melanoma are essential to minimizing morbidity and mortality. The presence of lymph node metastases is a vital prognostic predictor, and accurate identification by imaging has important implications for disease staging, prognosis, and clinical outcome. Sentinel lymph node (SLN) mapping procedures are limited by a lack of intraoperative visualization tools that can aid accurate determination of disease spread and delineate nodes from adjacent critical neural and vascular structures. Newer methods for circumventing these issues can exploit a variety of imaging tools, including biocompatible particle-based platforms coupled with portable device technologies for use with image-guided surgical and interventional procedures. We describe herein a clinically-translated, integrin-targeting platform for use with both PET and optical imaging that meets a number of key design criteria for improving SLN tissue localization and retention, target-to-background ratios, and clearance from the site of injection and the body. The use of such agents for selectively probing critical cancer targets may elucidate important insights into cellular and molecular processes that govern metastatic disease spread. Coupled with portable, real-time optical camera systems, we show that pre-operative PET imaging findings for mapping metastatic disease in clinically-relevant larger-animal models can be readily translated into the intraoperative setting for direct visualization of the draining tumor lymphatics and fluorescent SLN/s with histologic correlation. The specificity of this platform, relative to the standard-of-care radiotracer, ^{18}F-FDG, for potentially discriminating metastatic disease from

Correspondence to: Michelle S. Bradbury, bradburm@mskcc.org.

†These authors contributed equally to this work.

inflammatory processes is also discussed in the setting of surgically-based or interventionally-driven therapies.

Introduction

Malignant melanoma is one of the fastest rising cancers in the US, and is estimated to rise by 1% every year. The incidence rate of melanoma has risen 3-fold in the US over the past 3 decades, with similar rates reported in Europe. The highest incidence rates have been reported from Australia and New Zealand (40 to 60 cases per 100 000 inhabitants and year). The American Cancer Society estimated that there were will be 76 250 new melanoma cases diagnosed in 2012, resulting in 12 190 deaths;[1] in the United States, it now ranks the fifth most common cancer in males and sixth most common in females. Prognosis is largely determined by thickness and ulceration of primary tumor. However, the presence of lymph node metastases is the most important prognostic predictor[2] and considerable effort goes into examining the regional lymph nodes for the presence of lymphatic metastasis.

Early diagnosis and treatment are essential to minimizing morbidity and mortality. Definitive treatment for primary cutaneous melanoma is surgical resection in the form of a wide local excision. Adjuvant radiation is added for specific indications including locally invasive tumors and/or spread to multiple regional lymph nodes. There are no currently accepted standard-of-care systemic treatment options available. However, systemic treatment of melanoma is available in the clinical trials setting and is only offered to patients based on regional node risk stratification (*i.e.*, SLN mapping). It is therefore essential to accurately stage melanoma in its earlier phases by carefully examining regional nodes for metastatic disease spread. The use of molecular imaging tools,[3] including intraoperative probes, may aid in this process, improving disease visualization and staging during SLN biopsy procedures, while reducing the risk of lymphedema and other side effects of more extensive node dissection by harvesting only disease-bearing nodes.

SLN mapping and biopsy: current clinical practice

SLN mapping techniques, routinely used in staging melanoma, specifically identify the node/s that drain the primary tumor and are at highest risk of tumor metastases. The identification of lymph node metastases permits patients to be stratified to appropriate treatment arms in a more timely fashion, and can thereby potentially improve patient outcomes.

Non-invasive imaging methods, such as CT, MRI, positron emission tomography (PET), or combinations thereof, have been used to identify cancerous spread by screening for abnormally enlarged and/or metabolically active nodes. In the latter case, different tumor types demonstrate enhanced glucose metabolism and overexpression of glucose transporters (GLUTs); this is typically revealed using the glucose mimetic, 2-deoxy-2-[^{18}F]fluoro-D-glucose (^{18}F-FDG).[4] However, ^{18}F-FDG PET avidity is not specific or reliable, as nodal enlargement can be seen with inflammatory, infectious, or other metabolically active processes, and may co-exist with the spread of cancerous cells. Further, nodes smaller than a defined size threshold (*i.e.*, 1.5 cm) may harbor micrometastases that are not evident by

traditional ^{18}F-FDG PET. Finally, an inability to translate sites of metastatic disease seen on these pre-operative planning studies into three-dimensional (3D) locations during the surgical procedure poses major challenges for intraoperative identification, precluding direct mapping of locoregional nodal distributions within an exposed nodal basin. For these reasons, a combination of these techniques along with newer cancer-targeted approaches has been developed to enable the translation of pre-operative findings to the operative field, facilitating SLN localization.

Standard-of-care SLN mapping techniques rely on the uptake of an imaging agent, injected about the primary tumor site, for transport to the SLN *via* one or more lymphatic channels (Fig. 1a). One such agent, filtered technetium-radiolabeled sulfur colloid (*i.e.*, ^{99m}Tc-sulfur colloid) is injected pre-operatively for SLN localization and visualized with a gamma camera co-registered to a CT scan for spatial orientation. Intraoperatively, a hand-held gamma probe is used to measure radioactivity in the draining lymphatic structures, and help the surgeon localize the SLN. SLN mapping with ^{99m}Tc-sulfur colloid radiotracer is standard-of-care procedure for staging the regional nodal basin in early melanoma (~50 000 procedures per year in US). Another intraoperative adjunct for localizing SLNs is isosulfan (Lymphazurin 1%, US Surgical, North Haven, CT) or ‘blue dye’, which turns the SLN blue following injection into the peritumoral region and allows visual identification of a “hot and blue” SLN.

Current SLN mapping and biopsy techniques suffer from several drawbacks. Primarily, spatial resolution is low, offering no real time visualization or detailed anatomy of nodes and lymphatic channels within the operative field. In addition, filtered ^{99m}Tc-sulfur colloid particles, ranging in size from 10–100 nm, demonstrate slow clearance from the site of injection (*i.e.*, interstitial space), which can effectively limit adequate visualization of the draining lymphatics. Although the SLN may be radioactive and “hot” to the intraoperative gamma probe, the operating surgeon needs to rely principally on an abnormal visual appearance and palpation to discriminate the SLN and reliably differentiate it from adjoining tissues. If adjunctive blue dye injection is used, the blue SLN is apparent only if it is located superficially in the operative field and may not become apparent until significant amount of tissue dissection has taken place. Moreover, intraoperative identification of SLNs which can be 4–5 mm in size is fraught with the risk of injury to important adjacent structures such as nerves and vessels. Within certain areas of the body such as the head and neck, injury to neurovascular structures can result in dramatic consequences and can permanently alter functions such as speech and swallowing, and the cosmetic appearance of the patient. Within the head and neck, failure to identify any drainage pattern or localize small nodes occurs in up to ~10% of cases.[5] Staging of head and neck melanomas has been hampered by unpredictable patterns of metastatic disease spread, difficult-to-detect nodes in anatomic proximity to tumor, and difficulty in intraoperative differentiation of small nodes from vital structures during surgery.

Near-infrared fluorophores for SLN mapping

The limitations associated with standard-of-care SLN mapping techniques, along with innovations in contrast agent development and imaging technologies (*i.e.*, optical, PET-CT,

MRI), have spurred efforts to develop new tools for improving lymphatic imaging strategies and identify the SLN/s for biopsy. Traditional near-infrared (NIR) organic dyes (*e.g.*, Cy7, Cy5.5) are frequently used to map the lymphatic system, but have associated drawbacks. Dyes are prone to extravasation into the surrounding tissues given their small size and require conjugation to macromolecules (*i.e.*, proteins, immunoglobulins) for retention within the lymphatic system. Their reduced brightness and photostability decrease useful imaging penetration depths, and their relatively wide emission spectra can result in destructive spectral interference, precluding their use in multispectral imaging applications.[6] The FDA-approved NIR dye indocyanine green (ICG, emission peak ~830 nm) is a commonly used fluorophore in clinical settings[7,8] to image lymphatic flow and SLN/s at very low doses.[7] However, the versatility of this agent is limited, and the absence of functional groups can make conjugation to targeting and/or contrast-producing moieties challenging.[9] Given the weak and unstable nature of this NIR dye, depth penetration is restricted, with detection largely confined to interrogation of superficial nodes.

Newer generation technologies for image-guided surgery and interventions

Newer-generation molecular and particle-based agents, such as non-targeted activatable[10–12] and targeted organic fluorophores,[13–15] gadolinium labeled dendrimers[16–18] and other nanocarriers,[19] and macromolecular agents,[20–22] have been developed for use with image-guided procedures. A detailed discussion of each of these classes of agents is beyond the scope of this article, but a number of excellent reviews[9,18,23–29] are available relating to this subject. The more recent introduction of multimodal nanoparticles[30–32] for use with at least two imaging modalities can potentially improve lymph node resection efforts by aiding pre-operative planning and intraoperative guidance on the basis of a single platform technology. Such dual-modality agents, coupled with increasingly sensitive and higher resolution portable optical imaging devices permitting on-the-fly adjustments to image quality during acquisition, enable real-time image-guided treatment to be placed under the direct control of the operating surgeon or interventionalist. Under these conditions, sites of disease on pre-operative imaging scans might be more readily translated into 3D locations within the exposed operative bed during surgical procedures. Confirmation of tissue fluorescence can be obtained by hand-held PET probes for gamma and/or beta ray detection. This set-up would further enable the surgeon to see metastatic SLN/s through overlying tissue in order to accurately delineate these node(s) from adjoining anatomy, thereby minimizing risk of injury to crucial structures such as blood vessels and nerves.

For lymphatic imaging, ideal imaging agents should exhibit key properties that improve SLN tissue localization and retention (*i.e.*, surface receptor binding, internalization), enhance imaging signal at the target site, and promote more rapid clearance from the site of injection and the body in order to maximize target-to-background ratios (*i.e.*, agent should target and clear). The need to minimize normal-tissue radiation dose is a further consideration for radiotracers. For mapping lymphatic tumor spread using particle-based agents, key design constraints need to be met to achieve maximum diagnostic/therapeutic benefit while minimizing associated complications (*i.e.*, injury to adjacent critical structures, lymphedema).

Cancer-targeting, dual-modality core shell silica nanoparticles

Fluorescent core–shell silica nanoparticles (Cornell or C dots)[33,34] were designed for use in nanomedicine applications, including SLN mapping. This particle technology was modified with small numbers of peptide ligands, cyclic arginine-glycine-aspartic acid-tyrosine (cRGDY), attached to short, particle-bound, methoxyterminated polyethylene glycol chains (PEG ~0.5 kDa)[35] to create a non-toxic, potent high affinity integrin-targeting probe.[32] Peptide ligands were labeled with the positron-emitting radionuclide, iodine-124 (^{124}I), through the use of a tyrosine linker to create a dual-modality (optical-PET) platform, ^{124}I-cRGDY-PEG-C dots (Fig. 1b). This platform technology is ideally suited for SLN mapping and other image-guided applications based on the following design considerations: (1) small size, with tunable radius down to ~4.0 nm, for optimizing clearance profiles[33] and promoting more uniform delivery into nodes and other metastatic disease sites; (2) targeting peptides for tumor-selective uptake, accumulation, and retention in integrin-expressing tumors, including malignant melanoma cells and xenografts; [32] (3) encapsulated organic dyes (*i.e.*, Cy5.5; emission maxima, ~694 nm) for dramatically enhancing photophysical features, such as brightness (>200% relative to a free dye) and photostability relative to the parent dye in aqueous solutions; (4) PEG-coated surfaces for reducing non-specific uptake by the liver, spleen, bone marrow; and (5) versatility of the silica shell for permitting multiple functions to be combined as a single vehicle, creating highly functionalized particle platforms.

We present the results of utilizing this first FDA investigational new drug approved dual-modality silica particle (~6–7 nm diameter) for improving the detection and localization of SLN metastases, differentiating nodal tumor burden, and monitoring treatment response to image-guided ablation procedures in a well-established spontaneous melanoma miniswine model[36] using both PET and optical imaging approaches. This inorganic platform, defining a distinct class of theranostic platforms for nanomedicine,[37] has recently been found to be safe in our first-in-human clinical trial in metastatic melanoma patients.[38] For our SLN mapping studies, pre-operative and intraoperative imaging findings were correlated with histologic and immunochemical assays to confirm the presence or absence of melanoma. We illustrate the specificity of this platform, relative to the standard-of-care radiotracer, ^{18}F-FDG, for cancer staging and for discriminating metastatic disease from inflammatory processes. Following local injection of this PET-optical particle probe about the primary tumor site in these miniswine models, we show that pre-operative PET imaging findings for mapping metastatic disease can be successfully translated to the intraoperative setting using a state-of-the-art, high-resolution, hand-held fluorescent camera system, the ArteMIS™ system, for direct, real-time visualization of the draining tumor lymphatics and fluorescent SLN/s. Optical localization of the particle was confirmed using a clinically-approved hand-held PET probe (IntraMedical Imaging LLC, Los Angeles, CA) for detecting gamma emissions prior to lymph node resection. The results of these studies highlight key design criteria which are needed to achieve optimal tumor-localizing properties of this particle platform within metastatic nodes, accurately image the lymphatic system, and promote local and whole body clearance.

Design considerations for translatable particle platform technologies

Particle size

Particle size is one of the critical determinants of lymphatic uptake kinetics. Smaller particles should lead to a more rapid migration from the interstitial space into the lymphatic system. This property may enable delineation of a greater number of smaller caliber lymphatic channels, as well as produce higher contrast images. A smaller particle size is an appealing feature for enhanced delivery of probes into tumor-bearing nodes, and might additionally extend the lower limit of nodal sizes that can be sensitively detected. However, particle sizes less than about 3 nm (including dyes) are prone to extravasation and nonspecific tissue dispersal, increasing background fluorescence and potentially prolonging retention within the interstitium.[33,39,40] Furthermore, such small particles demonstrate enhanced rates of efflux from tumor-bearing tissues, reducing nodal retention. For increasingly larger particle sizes, slower physiologic transport within cancer-infiltrated tissues may hinder a more uniform diffusion of particles throughout the interstitium, although target selectivity may be increased.[23]

Circulation lifetimes and clearance

The size of particle platforms will affect their circulation or residence half-times. Assuming a non-toxic platform, longer blood half-times (<600 min)[23] may be needed to increase the potential for sensitively targeting metastatic disease and discriminating tumor burden within more solid, tumor-bearing nodes. For diagnostic studies, this consideration should be weighed against the need to promote more rapid whole body clearance, preferably through the kidneys. Ultrasmall particle-based platforms or macromolecular systems that meet effective renal glomerular filtration size cutoffs of 10 nm or less are desirable.[41] Particles larger than about 10 nm diameter will progressively accumulate in the liver, followed by eventual hepatobiliary excretion. While ultimately effective, this mode of clearance prolongs exposure to administered particle loads, increasing the potential for adverse effects or toxicity.

Cellular/tissue targeting and uptake

Selectivity of most cancer-directed particle probes principally relies on the enhanced permeability and retention (EPR) effect,[23,42] a passive solid tumor targeting process that results in preferential uptake and penetration of agents in tumor tissue relative to normal tissues. Longer circulation half-times are desirable to increase penetration. This property, found for many particle-based agents, promotes extravasation across more highly permeable tumor vasculature and effective diffusion through the tumor interstitium. Further, a number of critical tumor targets (*e.g.*, cathepsins, vascular endothelial growth factor receptor, matrix metalloproteinases) known to be highly expressed by malignant cancer cells and the tumor microenvironment, as well as associated with key hallmarks of cancer,[43] may serve to improve targeted detection of malignant cells and tissues using a variety of agents (*i.e.*, peptides, antibodies and nanoparticles). Enhanced penetration and retention times have been observed for some of these targeted particle platforms relative to non-targeted particles.[23,44,45] Collectively, these properties enhance imaging detection sensitivity and specificity, and may permit discrimination of tumor-infiltrated nodal tissue from normal

tissue[46,47] or other disease processes (inflammation, infection) that similarly manifest as nodal enlargement.

The aforementioned targets, as well as $\alpha_v\beta_3$ integrin, the target used in our studies, and whose overexpression promotes sustained angiogenesis, can be identified using small surface-bound ligands which specifically recognize and bind to tumor neovasculature and cancer cells. We showed high binding specificity of cRGDY-PEG-C dots to integrin surface receptors of M21 human melanoma cells by flow cytometry (Fig. 2a), and this was accompanied by retention of the particle and persistent imaging signal in M21 xenografts.[32] *In vitro* assays showed complete blocking of receptor-mediated binding using anti-$\alpha_v\beta_3$ integrin antibody (Fig. 2a). Along with surface binding, the internalization of integrin-targeting agents *via* receptor-mediated endocytosis or other internalization gateway has been observed in M21 (Fig. 2) and other $\alpha_v\beta_3$ integrin positive tumor cells,[48] leading to slower probe clearance and net tumor accumulation relative to surrounding tissues.

In order to identify the biological compartments involved in cRGDY-PEG-C dot internalization, we performed colocalization assays in M21 cells with cRGDY-PEG-C dots and biomarkers of different endocytotic vesicles. Internalization of the targeted particle (~1 micromolar, red, 4-hr incubation) was sensitively detected by an inverted confocal microscope (Leica TCS SP2 AOBS) equipped with a HCX PL APO objective (63 × 1.2NA Water DIC D) (Fig. 2b). Using endocytotic markers LysoTracker Red (100 nM, green) (Fig. 2c) and transferrin-Alexa488, uptake into acidic endocytic structures was confirmed, with the latter suggesting clathrin-dependent pathway activity[49] and gradual acidification of vesicles. Fig. 2d shows colocalization data between the particle and acidic endocytic vesicles (yellow puncta). Uptake into macropinocytes was also observed with 70 kDa dextran-FITC[49,50] (1 mg mL^{-1}), which co-localized with cRGDY-PEG-C dots (Fig. 2e); this finding, seen as yellow puncta, suggested a second pathway of internalization. Nuclear counterstaining (blue) was done with Hoechst 33258 (0.01 mg mL^{-1}). No particles entered the nucleus. Surface-bound particles were additionally noted (red, Fig. 2e).

Surface charge

Surface charge can affect the transport properties of particles across the vasculature and within the interstitium. Particles having a net surface charge may be opsonized by serum proteins,[33,51] effectively increasing probe size and preventing renal excretion. By attaching PEG chains to the particle surface to create chemically neutral surfaces and bioinert platforms, uptake by other cells is largely prevented and particles will effectively be excreted by the kidneys. Furthermore, compared to its charged counterparts, a more neutrally-charged surface will increase diffusion and lead to a more homogeneous distribution within the interstitial space of cancer-infiltrated tissues.[23]

Brightness and photostability

Fluorescence probes (*e.g.*, organic dyes, fluorescent proteins, dye-bound proteins/macromolecules, dye-containing nanoparticles) have enhanced imaging evaluations of the lymphatic system in the intraoperative setting, facilitating localization of the SLN/s, draining tumor lymphatic channels, and enabling the simultaneous visualization of nodal

distributions[6] from different draining regions. Newer generation probes that emit in the NIR region (650–900 nm) exhibit decreased tissue attenuation and autofluorescence from nontarget tissues, thereby maximizing target to background ratios and offering improved, but overall low, depth penetration (3–4 millimeters) relative to visible emitters. [18] By covalently incorporating organic dyes (*i.e.*, Cy5.5) into the silica matrix of our particle probe to prevent dye leaching, [33,35] notable photophysical enhancements over the free dye have been observed. Silica encapsulated dye molecules were found to exhibit significant increases in brightness (200–300%) and extended photostability (2–3 fold increases) compared with the free dye.[33] Higher penetration depths have also been found in our *in vivo* SLN mapping studies using a state-of-the-art fluorescence camera system (described below), with our particle visible through a maximum of 2 cm of tissue. These unique photophysical features, in conjunction with state-of-the-art fluorescence camera systems, allow for exciting possibilities in the staging and future treatment of cancer.

Image-guided surgery: ArteMIS™ fluorescence imaging system

One such intraoperative imaging device, the ArteMIS™ hand-held fluorescence camera system (Quest Medical Imaging, Middenmeer, The Netherlands) (Fig. 3a), has been adapted for both minimally invasive laparoscopic (Fig. 3b and c) and open surgical procedures, (Fig. 3c). It is the first hand-held, multi-channel fluorescence imaging camera for intraoperative imaging guidance, producing high-resolution visible (color) images and fine-tuned near-infrared (NIR) fluorescent signals, which are simultaneously acquired in real-time. This capability allows for motion-free overlaying. This hand-held device is optimal for SLN mapping procedures, as it can be easily positioned to view otherwise difficult anatomic locations, such as the head and neck. More importantly, the capability of acquiring simultaneous images of different fluorescence wavelengths (*i.e.*, multispectral imaging) enables a completely new approach of utilizing fluorescence imaging guidance for surgical and interventional procedures. All sensors in the device are physically aligned such that the single axis lens delivers images of the specifically tuned wavelength to the appropriate sensor. Filtering out the required wavelength of interest, as well as being able to individually control each of these sensors, which are triggered to start acquiring photons at exactly the same time and same viewing position, is of great importance. The tight integration of the light engine, controllable from the camera system, allows optimization based on imaging feedback.

This CE-certified, FDA-exempt system has been used in larger animal studies described below, and will be integrated, along with our dual-modality particle, into future planned SLN mapping clinical trial protocols. To confirm that detected optical signal at sites of particle localization *in vivo* was not simply autofluorescence, reflecting intrinsic fluorescence of tissue structures activated by light of suitable wavelengths, a portable gamma probe, calibrated for I-124, was utilized to measure detected gamma emissions prior to lymph node resection (Fig. 3d). Prior to initiating *in vivo* studies, a serial dilution study was performed using 10 nm Cy5.5-containing cRGDY-PEG-C dots, along with the portable camera system, to measure changes in optical signal as a function of particle concentration (Fig. 3e).

Nanomedicine applications

Dual-modality silica nanoparticles for image-guided intraoperative SLN mapping

We evaluated the feasibility of using ^{124}I-cRGDY-PEG-C dots and combined PET-optical imaging approaches for SLN mapping in a spontaneous melanoma miniswine model[36,52,53] (Sinclair miniature swine, Sinclair Research Center). Image-guided metastatic disease detection, staging, and the assessment of differential tumor burden in SLN/s were evaluated in 4–10 kg miniswine (n = 5) in conjunction with correlative histopathology. The results of these studies, described below, suggested that ^{124}I-cRGDY-PEG-C dots enabled superior detection sensitivity and discrimination of metastatic tumor burden within hypermetabolic neck nodes relative to ^{18}F-FDG. In all miniswine, dynamic 1 h high-resolution and whole body ^{18}F-FDG PET-CT scans were performed following systemic injection of 5 millicuries (mCi) ^{18}F-FDG to screen for metastatic disease, prior to ^{124}I-cRGDY-PEG-C dot administration. In a representative animal, a hypermetabolic melanomatous lesion and PET-avid right-sided SLN were initially identified in the posterior neck (Fig. 4a). Two days later, ^{124}I-cRGDY-PEG-C dots (~0.5 mCi, >95% purity) were administered as a 4-quadrant, subdermal injection dose about the tumor site. High resolution and whole body dynamic PET scans confirmed the prior ^{18}F-FDG imaging findings 5 minutes after injection, with the additional identification of 2 PET-avid nodes (Fig. 4b), one within the left posterior neck and a second immediately anterior to the SLN. No other PET-avid nodes or suspicious areas of tracer uptake were seen.

Imaged nodes were confirmed intraoperatively within the exposed surgical bed by visual inspection and γ-counting using hand-held PET devices prior to excision. Excised gross nodal specimens showed a black-pigmented (melanin-containing) SLN measuring 1.3 × 1.0 × 1.5 cm^3 (Fig. 4c), as compared with the smaller (1.0 × 0.6 × 1.0 cm^3) posterior, left-sided PET-avid node (Fig. 4d). H&E-stained SLN tissue sections revealed dark melanomatous clusters on low-power views (Fig. 4e) comprised of both melanoma cells and melanin-containing macrophages (*i.e.*, melanophages) on high-power views (Fig. 4f). These findings were similar to those for excised primary lesions (data not shown). Immunohistochemical staining of the SLN with a known human melanoma marker, HMB-45, demonstrated positive expression of this marker on low-power (Fig. 4g) and high-power views (Fig. 4h). By contrast, low-power (Fig. 4i) and high-power (Fig. 4j) views of H&E stained sections from the left-sided PET-avid node showed a few smaller sized melanomatous clusters containing melanoma cells and melanophages. Tumor burden in this smaller node, estimated to be 10- to 20-fold less than in the SLN by pathological analysis, was sensitively discriminated by the targeted particle probe. Representative normal-appearing porcine nodal tissue harvested from the neck revealed no metastatic infiltration in low-power (Fig. 4k) and high-power (Fig. 4l) views.

These studies were expanded to include optical imaging using the portable ArteMIS™ fluorescence camera system, along with radiodetection using the gamma probe, for performing real-time assessments of the draining tumor lymphatics and nodal metastases. In a representative miniswine (Fig. 5), initial pre-operative PET-CT scanning was performed using ^{18}F-FDG and ^{124}I-cRGDY-PEG-C dots using the following procedure. Axial CT

images revealed a primary pelvic tumor (Fig. 5a) and draining SLN (Fig. 5b), which were seen as areas of increased activity on the corresponding ^{18}F-FDG PET scan (Fig. 5c and d). These findings were confirmed 2 days later by dynamic PET-CT imaging about 5 minutes after subdermal, 4-quadrant injection of ^{124}I-cRGDY-PEG-C dots about the tumor site; co-registered axial (Fig. 5e and g) and coronal (arrows, 5f, 5h) views demonstrate these findings. Following pre-operative scanning, the skin overlying the SLN site was marked for intraoperative localization, and the miniswine was transported to the intraoperative suite. Baseline activity measurements, made over the primary tumor and SLN sites using the portable gamma probe (Fig. 5i), showed a 20-fold increase in activity within the SLN relative to background signal.

For real-time optical imaging of the lymphatic system, a second subdermal injection of ^{124}I-cRGDY-PEG-C dots was administered about the tumor site with the skin intact, and the signal viewed in the color (Fig. 6a) and Cy5.5 fluorescent channels (Fig. 6b). The adjacent nodal basin was exposed, and fluorescent signal was seen in the NIR channel flowing from the injection site (Fig. 6c) into the main proximal (Fig. 6c and d), mid (Fig. 6e), and distal (Fig. 6f) lymphatic branches, which drained towards the SLN (Fig. 6f). Smaller caliber lymphatic channels were also visualized (Fig. 6d and e). The black-pigmented SLN, viewed in dual-channel mode (Fig. 6g and h), was further exposed (Fig. 6i) prior to successive nodal excision (Fig. 6j–m). Fluorescence signal within the *in situ* (Fig. 6k) and *ex vivo* (Fig. 6m) nodal specimen was confirmed by gamma emissions using the gamma probe (Fig. 5i), and seen to correspond to scattered clusters of tumor cells on low-power (box, Fig. 6n) and high-power (Fig. 6o) views from H&E-stained tissue sections. Positive expression of HMB-45 was identified on low-power (Fig. 6p) and high-power (Fig. 6q) views, consistent with metastatic melanoma.

Surprisingly, and by contrast to the observed ^{18}F-FDG findings, ^{124}I-cRGDY-PEG-C dots were found to specifically discriminate between metastatic tumor infiltration and inflammatory processes in these miniswine. Mechanistic differences in the behavior of these agents at the cellular and subcellular levels, as well as the presence of an integrin-targeting moiety on the particle surface, may account for the observed imaging findings. In multiple miniswine harboring pathologically-proven inflammatory changes due to granulomatous disease ($n = 3$), ^{18}F-FDG failed to detect metastatic disease, while identifying inflammatory and other metabolically active sites. These discrepant findings highlighted the ability of ^{124}I-cRGDY-PEG-C dots to selectively target, localize, and stage metastatic disease, while ^{18}F-FDG failed in many cases to accurately stage cancer spread, instead identifying sites of inflammation.

In a representative miniswine study illustrating these findings, initial axial ^{18}F-FDG PET-CT scans showed calcification within the left posterior neck on CT (Fig. 7a), corresponding to an area of intense activity on the ^{18}F-FDG PET (Fig. 7b). Low-power (Fig. 7c) and high-power (Fig. 7d) views of H&E stained tissue sections revealed diffuse inflammatory changes, consistent with granulomatous disease. Intense ^{18}F-FDG PET activity was additionally seen within the metabolically active bone marrow compartment of these young miniswine (Fig. 7a and b). By contrast, the ^{124}I-cRGDY-PEG-C dot imaging study identified bilateral metastatic neck nodes. A right neck node on axial CT imaging (Fig. 7e)

was seen to be PET-avid on co-registered PET-CT (Fig. 7f); additional bilateral nodes on a more superior CT image (Fig. 7g) were also PET-avid on fused PET-CT (Fig. 7h). Moreover, left neck calcifications (Fig. 7e and g) showed no PET activity on co-registered scans (Fig. 7f and h). Corresponding H&E-stained SLN tissue sections revealed dark melanomatous clusters on low-power (box, Fig. 7i) and high-power views (Fig. 7j), seen to be comprised of melanoma cells and melanophages. A single frame (Fig. 7k) selected from 3D PET reconstructed images again illustrated multiple, bilateral PET-avid neck nodes and associated draining lymphatic channels. Importantly, bulk activity was seen in the bladder 1 h post-injection without significant tracer accumulation over the liver region.

The above findings were seen to better advantage on PET-CT fusion MIP images generated from dynamic imaging data sets acquired over a 1 hour period after ^{18}F-FDG (Fig. 8a) or local administration of ^{124}I-cRGDY-PEG-C dots (Fig. 8b and c). For ^{18}F-FDG, a clear absence of nodal metastases is noted, with diffusely increased activity seen within metabolically-active bony structures. In contrast to these findings, ^{124}I-cRGDY-PEG-C dots detected bilateral metastatic neck nodes, along with draining lymphatic channels.

Dual-modality silica nanoparticles for image-guided interventions: treatment response

The ability of the ^{124}I-cRGDY-PEG-C dots to discriminate metastatic disease from tissue inflammatory changes could potentially be exploited in a variety of therapeutic settings – either surgically-based or interventionally-driven – as treatment response assessments are often confounded by the presence of inflammatory changes, making interpretation difficult. Image-guided interventions, such as therapeutic tumor ablations, may specifically benefit from the innovative coupling of new particle platform and imaging device technologies to (1) enable earlier post-procedural evaluation of response; (2) verify complete ablation or detect residual tumor representing treatment failure, and (3) improve tumor surveillance strategies. Locally ablative therapies, including microwave ablation,[54] cryoablation,[55] radiofrequency ablation (RFA),[56–59] and laser interstitial therapy, induce local thermal injury *via* an energy applicator insertion into tumors. These methods are typically employed as alternative options in patients deemed ineligible for surgical excision.[60,61] Further, patients undergoing ablative therapies are often poor surgical candidates due to co-morbidities. Widely used in clinical practice, they offer a distinct advantage, as they can be performed percutaneously as outpatient procedures with significantly less morbidity, and may improve quality of life and survival in selected patient cohorts.[61,62]

Accurate post-therapy imaging, typically acquired 1–3 months after an ablation procedure, traditionally utilized contrast-enhanced volumetric imaging, such as CT or MRI.[60–62] These techniques suffer from a number of drawbacks. First, they are limited to identifying the presence of abnormal enhancement or growth in the size of the tumor area,[61] considered primary indicators of residual tumor or recurrent disease. Diffuse rim enhancement about the ablation zone on post-procedural evaluations may be related to inflammation and hyperemia in the ablation zone, and often does not necessarily represent residual tumor.[62] Increasing enhancement, notably irregular or nodular, is considered suspicious for tumor. However, these interpretations are controversial, as an ablation zone can look larger than expected for several months post-procedure, and enhancement might also reflect granulation or scar

tissue formation.[62,63] Functional methods, such as ^{18}F-FDG PET, have also been used to assess the efficacy and effects of locally ablative procedures, but may suffer from an inability to accurately discriminate tumor from inflammatory changes. Thus, interpretation of imaging changes (*i.e.*, inflammation, tumor) at the tissue level in response to ablative procedures using current morphologic or functional assessments, particularly at early time intervals, is a significant challenge. What is needed are reliable endpoints for ablation success and unequivocal detection of residual disease in the post-ablation period.

As a forerunner to performing future ablations of metastatic liver lesions, a proof-of-concept radiofrequency ablation (RFA) study of a larger (*i.e.*, 1–2 cm) SLN was performed in a miniswine with metastatic melanoma to evaluate early treatment response in the presence of ^{124}I-cRGDY-PEG-C dots. PET-CT imaging findings prior to and after RFA were correlated histologically. Following subdermal injection of ^{124}I-cRGDY-PEG-C dots (~0.6 mCi) about the primary left pelvic tumor, an initial baseline coronal CT showed a 2.2 × 1.6 cm SLN (Fig. 9a) superior to the tumor site, which was PET-avid (Fig. 9b and c). The PET-avid left pelvic tumor is also shown (Fig. 9b), noting additional flow of ^{124}I-cRGDY-PEG-C dots within a draining lymphatic channel on fused PET-CT images (Fig. 9c and d). Additional serial CT scans were acquired to localize the node (Fig. 9e) prior to the ablation procedure and guide RFA probe insertion (Fig. 9f) into the node (below level of crosshairs). On the corresponding pre-ablation co-registered PET-CT scan, the PET-avid SLN was seen just posterior to crosshairs (Fig. 9g). A partial node ablation was performed for 12 minutes using a 2 cm active tip RFA probe (Cool-tip ablation system, Covidien plc, Dublin, Ireland). Postablation PET-CT showed mildly reduced tracer activity in the ablation zone, anterior to the electrode tip (Fig. 9h).

Pre- and post-ablation imaging findings were confirmed histologically. H&E staining of pre-ablated core biopsy tissue from the SLN confirmed diffuse metastatic tumor infiltration on low-power (Fig. 9i) and high-power (Fig. 9j) views. Post-ablation, the extent of metastatic infiltration decreased on H&E stained nodal tissue, seen on corresponding low- (Fig. 9k) and high-power views (Fig. 9l). Coagulative necrosis and lymphoid tissue were also identified, along with multifocal hemorrhages (Fig. 9k and l, respectively). TUNEL stained high-power views prior to ablation reveal scattered neoplastic cells (Fig. 9m). On post-ablation TUNEL staining, focal areas of necrosis (red) were seen on both low- (Fig. 9n) and high-power (Fig. 9o) views.

Conclusions

Lymph node metastases are a powerful predictor of outcome for melanoma. Early detection of micrometastases in regional lymph nodes using SLN mapping may permit the timely stratification of patients to appropriate treatment arms, and can potentially improve patient outcomes. Although the current standard-of-care SLN mapping and biopsy techniques rely on the use of radioactivity-based identification of SLN/s, a number of limitations of this technology exist. These include low spatial resolution, reduced staging accuracy, absence of target specificity, slow tracer clearance that may obscure the surgical field, and the lack of accurate intraoperative visualization to prevent injury to vital structures lying in close proximity to SLN/s.

The recent introduction of newer generation, biocompatible particle platforms that can be actively tailored and refined to overcome these drawbacks according to key design criteria, while enabling selective probing of critical cancer targets, can offer important insights into cellular and molecular processes governing metastatic disease spread. The additional adaptation of such platforms for multimodality imaging could be used to advantage by the operating surgeon or interventionalist to explore these processes in a variety of image-guided procedural settings. One such dual-modality platform, a clinically-translated integrin-targeting silica nanoparticle developed for both optical and PET imaging, meets a number of key design criteria – small size, superior brightness, enhanced tumor tissue retention, and low background signal – that make it an ideal agent for SLN localization and staging during SLN biopsy procedures when coupled with portable, real-time optical camera systems (*i.e.*, ArteMIS). The ability to discriminate metastatic disease from tissue inflammatory changes in melanoma models, which are often co-existing processes, may provide a more accurate and reliable marker for the assessment of treatment response in the future. Further investigation in a broader set of cancer types and treatments is warranted using either surgically-based or interventionally-driven therapies.

Acknowledgments

We acknowledge Hooisweng Ow for preparing and characterizing silica nanoparticles, Sander de Jonge for software development, and Sebastian Monette for pathological analysis. We would also like to thank Esa Tuominen, Steven M. Larson, Pat B. Zanzonico, Steven Solomon, William Strauss (Memorial Sloan-Kettering Cancer Center) as well as Shankar Vallabhajosula (Cornell University) for providing technical assistance. This work was supported by a New York City Investment Fund – BioAccelerate Award and an MSKCC Technology Development Fund Award to M.B. Technical services provided by the MSKCC Large-Animal Imaging Core Facility, supported in part by the NIH Center Grant No P30 CA08748, are gratefully acknowledged.

References

1. ACS Cancer Facts & Figures. Atlanta GA: 2012.
2. Balch CM, et al. Prognostic factors analysis of 17 600 melanoma patients: validation of the American Joint Committee on Cancer melanoma staging system. J Clin Oncol. 2001; 19(16):3622–3634. [PubMed: 11504744]
3. Weissleder R. Molecular imaging in cancer. Science. 2006; 312(5777):1168–1171. [PubMed: 16728630]
4. Kelloff GJ, et al. Progress and promise of FDG-PET imaging for cancer patient management and oncologic drug development. Clin Cancer Res. 2005; 11(8):2785–2808. [PubMed: 15837727]
5. Erman AB, et al. Sentinel lymph node biopsy is accurate and prognostic in head and neck melanoma. Cancer. 2012; 118(4):1040–1047. [PubMed: 21773971]
6. Kobayashi H, et al. Simultaneous multicolor imaging of five different lymphatic basins using quantum dots. Nano Lett. 2007; 7(6):1711–1716. [PubMed: 17530812]
7. Sevick-Muraca EM, et al. Imaging of lymph flow in breast cancer patients after microdose administration of a near-infrared fluorophore: feasibility study. Radiology. 2008; 246(3):734–741. [PubMed: 18223125]
8. Crane LM, et al. Intraoperative near-infrared fluorescence imaging for sentinel lymph node detection in vulvar cancer: first clinical results. Gynecol Oncol. 2011; 120(2):291–295. [PubMed: 21056907]
9. Rasmussen JC, et al. Lymphatic imaging in humans with near-infrared fluorescence. Curr Opin Biotechnol. 2009; 20(1):74–82. [PubMed: 19233639]
10. Keereweer S, et al. Detection of oral squamous cell carcinoma and cervical lymph node metastasis using activatable near-infrared fluorescence agents. Arch Otolaryngol, Head Neck Surg. 2011; 137(6):609–615. [PubMed: 21690514]

11. Mahmood U, Weissleder R. Near-infrared optical imaging of proteases in cancer. Mol Cancer Ther. 2003; 2(5):489–496. [PubMed: 12748311]
12. Wunderbaldinger P, et al. Near-infrared fluorescence imaging of lymph nodes using a new enzyme sensing activatable macromolecular optical probe. Eur Radiol. 2003; 13(9):2206–2211. [PubMed: 12802615]
13. Gleysteen JP, et al. Fluorescently labeled cetuximab to evaluate head and neck cancer response to treatment. Cancer Biol Ther. 2007; 6(8):1181–1185. [PubMed: 17637562]
14. Lee SB, et al. Affibody molecules for *in vivo* characterization of HER2-positive tumors by near-infrared imaging. Clin Cancer Res. 2008; 14(12):3840–3849. [PubMed: 18559604]
15. Withrow KP, et al. Assessment of bevacizumab conjugated to Cy5.5 for detection of head and neck cancer xenografts. Technol Cancer Res Treat. 2008; 7(1):61–66. [PubMed: 18198926]
16. Koyama Y, et al. A dendrimer-based nanosized contrast agent dual-labeled for magnetic resonance and optical fluorescence imaging to localize the sentinel lymph node in mice. J Magn Reson Imaging. 2007; 25(4):866–871. [PubMed: 17345640]
17. Kobayashi H, et al. Delivery of gadolinium-labeled nanoparticles to the sentinel lymph node: comparison of the sentinel node visualization and estimations of intra-nodal gadolinium concentration by the magnetic resonance imaging. J Controlled Release. 2006; 111(3):343–351.
18. Lucarelli RT, et al. New approaches to lymphatic imaging. Lymphatic Res Biol. 2009; 7(4):205–214.
19. Jain R, et al. Diagnostic nanocarriers for sentinel lymph node imaging. J Controlled Release. 2009; 138(2):90–102.
20. Wallace AM, et al. Lymphoseek: a molecular radiopharmaceutical for sentinel node detection. Ann Surg Oncol. 2003; 10(5):531–538. [PubMed: 12794019]
21. Hama Y, et al. Two-color lymphatic mapping using Ig-conjugated near infrared optical probes. J Invest Dermatol. 2007; 127(10):2351–2356. [PubMed: 17522707]
22. Povoski SP, et al. Multimodal Imaging and Detection Strategy With 124 I-Labeled Chimeric Monoclonal Antibody cG250 for Accurate Localization and Confirmation of Extent of Disease During Laparoscopic and Open Surgical Resection of Clear Cell Renal Cell Carcinoma. Surg Innov. 201210.1177/1553350612438416
23. Jain RK, Stylianopoulos T. Delivering nanomedicine to solid tumors. Nat Rev Clin Oncol. 2010; 7(11):653–664. [PubMed: 20838415]
24. Keereweer S, et al. Optical image-guided surgery--where do we stand? Mol Imaging Biol. 2011; 13(2):199–207. [PubMed: 20617389]
25. Sampath L, et al. Near infrared fluorescent optical imaging for nodal staging. J Biomed Opt. 2008; 13(4):041312. [PubMed: 19021320]
26. Schroeder A, et al. Treating metastatic cancer with nanotechnology. Nat Rev Cancer. 2012; 12(1): 39–50. [PubMed: 22193407]
27. Yudd AP, et al. Use of sentinel node lymphoscintigraphy in malignant melanoma. Radiographics. 1999; 19:343–353. [PubMed: 10194783]
28. Ravizzini G, et al. Nanoparticles in sentinel lymph node mapping. Wiley Interdiscip Rev: Nanomed Nanobiotechnol. 2009; 1(6):610–623. [PubMed: 20049820]
29. Khullar O, et al. Image-guided sentinel lymph node mapping and nanotechnology-basesd nodal treatment in lung cancer using invisible near-infrared fluorescent light. Semin Thorac Cardiovasc Surg. 2009; 21(4):309–315. [PubMed: 20226343]
30. Madru R, et al. 99mTc-labeled superparamagnetic iron oxide nanoparticles for multimodality SPECT/MRI of sentinel lymph nodes. J Nucl Med. 2012; 53(3):459–463. [PubMed: 22323777]
31. Olson ES, et al. Activatable cell penetrating peptides linked to nanoparticles as dual probes for *in vivo* fluorescence and MR imaging of proteases. Proc Natl Acad Sci U S A. 2010; 107(9):4311–4316. [PubMed: 20160077]
32. Benezra M, et al. Multimodal silica nanoparticles are effective cancer-targeted probes in a model of human melanoma. J Clin Invest. 2011; 121(7):2768–2780. [PubMed: 21670497]
33. Burns AA, et al. Fluorescent silica nanoparticles with efficient urinary excretion for nanomedicine. Nano Lett. 2009; 9(1):442–448. [PubMed: 19099455]

34. Choi J, et al. Core-shell silica nanoparticles as fluorescent labels for nanomedicine. J Biomed Opt. 2007; 12(6):064007. [PubMed: 18163823]
35. Burns A, et al. Fluorescent core-shell silica nanoparticles: towards "Lab on a Particle" architectures for nanobiotechnology. Chem Soc Rev. 2006; 35(11):1028–1042. [PubMed: 17057833]
36. Misfeldt ML, Grimm DR. Sinclair miniature swine: an animal model of human melanoma. Vet Immunol Immunopathol. 1994; 43(1–3):167–175. [PubMed: 7856049]
37. Jokerst JV, Gambhir SS. Molecular imaging with theranostic nanoparticles. Acc Chem Res. 2011; 44(10):1050–1060. [PubMed: 21919457]
38. Phillips E, Penate-Medina O, Zanzonico PB, Ow H, Carvajal RD, Mohan P, Ye Y, Humm J, Kalaigian H, Schoder H, Strauss WH, Larson SM, Wiesner U, Bradbury MS. Clinical Translation of an Ultrasmall Inorganic Fluorescent Hybrid Nanoparticle Probe. 2012 submitted.
39. Kobayashi H, et al. Multimodal nanoprobes for radionuclide and five-color near-infrared optical lymphatic imaging. ACS Nano. 2007; 1(4):258–264. [PubMed: 19079788]
40. Ohnishi S, et al. Organic alternatives to quantum dots for intraoperative near-infrared fluorescent sentinel lymph node mapping. Mol Imaging. 2005; 4(3):172–181. [PubMed: 16194449]
41. Choi CH, et al. Targeting kidney mesangium by nanoparticles of defined size. Proc Natl Acad Sci U S A. 2011; 108(16):6656–6661. [PubMed: 21464325]
42. Maeda H, et al. Tumor vascular permeability and the EPR effect in macromolecular therapeutics: a review. J Controlled Release. 2000; 65(1–2):271–284.
43. Hanahan D, Weinberg RA. The hallmarks of cancer. Cell. 2000; 100(1):57–70. [PubMed: 10647931]
44. Sugahara KN, et al. Tissue-penetrating delivery of compounds and nanoparticles into tumors. Cancer Cell. 2009; 16(6):510–520. [PubMed: 19962669]
45. Karmali PP, et al. Targeting of albumin-embedded paclitaxel nanoparticles to tumors. Nanomedicine. 2009; 5(1):73–82. [PubMed: 18829396]
46. Ke S, et al. Near-infrared optical imaging of epidermal growth factor receptor in breast cancer xenografts. Cancer Res. 2003; 63(22):7870–7875. [PubMed: 14633715]
47. Moon WK, et al. Enhanced tumor detection using a folate receptor-targeted near-infrared fluorochrome conjugate. Bioconjugate Chem. 2003; 14(3):539–545.
48. Kossodo S, et al. Dual *in vivo* quantification of integrin-targeted and protease-activated agents in cancer using fluorescence molecular tomography (FMT). Mol Imaging Biol. 2010; 12(5):488–499. [PubMed: 19960268]
49. Potocky TB, et al. Cytoplasmic and nuclear delivery of a TAT-derived peptide and a beta-peptide after endocytic uptake into HeLa cells. J Biol Chem. 2003; 278(50):50188–50194. [PubMed: 14517218]
50. Wadia JS, et al. Transducible TAT-HA fusogenic peptide enhances escape of TAT-fusion proteins after lipid raft macropinocytosis. Nat Med. 2004; 10(3):310–315. [PubMed: 14770178]
51. Moghimi SM, et al. Long-circulating and target-specific nanoparticles: theory to practice. Pharmacol Rev. 2001; 53(2):283–318. [PubMed: 11356986]
52. Oxenhandler RW, et al. Malignant melanoma in the Sinclair miniature swine: an autopsy study of 60 cases. Am J Pathol. 1979; 96(3):707–720. [PubMed: 474716]
53. Millikan LE, et al. Melanoma in Sinclair swine: a new animal model. J Invest Dermatol. 1974; 62(1):20–30. [PubMed: 4809019]
54. Lubner MG, et al. Microwave tumor ablation: mechanism of action clinical results, and devices. J Vasc Interv Radiol. 2010; 21(Suppl 8):S192–S203. [PubMed: 20656229]
55. Erinjeri JP, Clark TW. Cryoablation: mechanism of action and devices. J Vasc Interv Radiol. 2010; 21(Suppl 8):S187–S191. [PubMed: 20656228]
56. Abitabile P, et al. Radiofrequency ablation permits an effective treatment for colorectal liver metastasis. Eur J Surg Oncol. 2007; 33(1):67–71. [PubMed: 17174059]
57. Amersi FF, et al. Long-term survival after radiofrequency ablation of complex unresectable liver tumors. Arch Surg. 2006; 141(6):581–587. discussion 587–588. [PubMed: 16785359]

58. Farrell MA, et al. Imaging-guided radiofrequency ablation of solid renal tumors. AJR, Am J Roentgenol. 2003; 180(6):1509–1513. [PubMed: 12760910]

59. Hong K, Georgiades C. Radiofrequency ablation: mechanism of action and devices. J Vasc Interv Radiol. 2010; 21(Suppl 8):S179–S186. [PubMed: 20656227]

60. Anderson GS, et al. FDG positron emission tomography in the surveillance of hepatic tumors treated with radiofrequency ablation. Clin Nucl Med. 2003; 28(3):192–197. [PubMed: 12592125]

61. Purandare NC, et al. Therapeutic response to radiofrequency ablation of neoplastic lesions: FDG PET/CT findings. Radiographics. 2011; 31(1):201–213. [PubMed: 21257942]

62. Barker DW, et al. Evaluation of liver metastases after radiofrequency ablation: utility of 18F-FDG PET and PET/CT. AJR Am J Roentgenol. 2005; 184(4):1096–1102. [PubMed: 15788579]

63. Vogt FM, et al. Morphologic and functional changes in nontumorous liver tissue after radiofrequency ablation in an *in vivo* model: comparison of 18F-FDG PET/CT, MRI, ultrasound, and CT. J Nucl Med. 2007; 48(11):1836–1844. [PubMed: 17942811]

Insight, innovation, integration

Early detection of melanoma micrometastases in regional lymph nodes using sentinel lymph node (SLN) mapping and biopsy (SLNB) can potentially improve patient outcomes. Current SLNB technique has several limitations, including lack of intraoperative visual discrimination of the SLN from adjoining critical structures, including nerves and vessels. Newer generation, biocompatible particle imaging platforms can overcome these drawbacks for use in a variety of image-guided applications while selectively probing critical cancer targets. One such dual-modality optical-PET platform, a clinically-translated, integrin-targeting silica nanoparticle, meets a number of key design criteria when coupled with PET and portable, real-time optical camera systems. Its ability to discriminate metastatic disease from tissue inflammatory changes in melanoma models may provide a more accurate and reliable modality for surgically-based or interventionally-driven therapies.

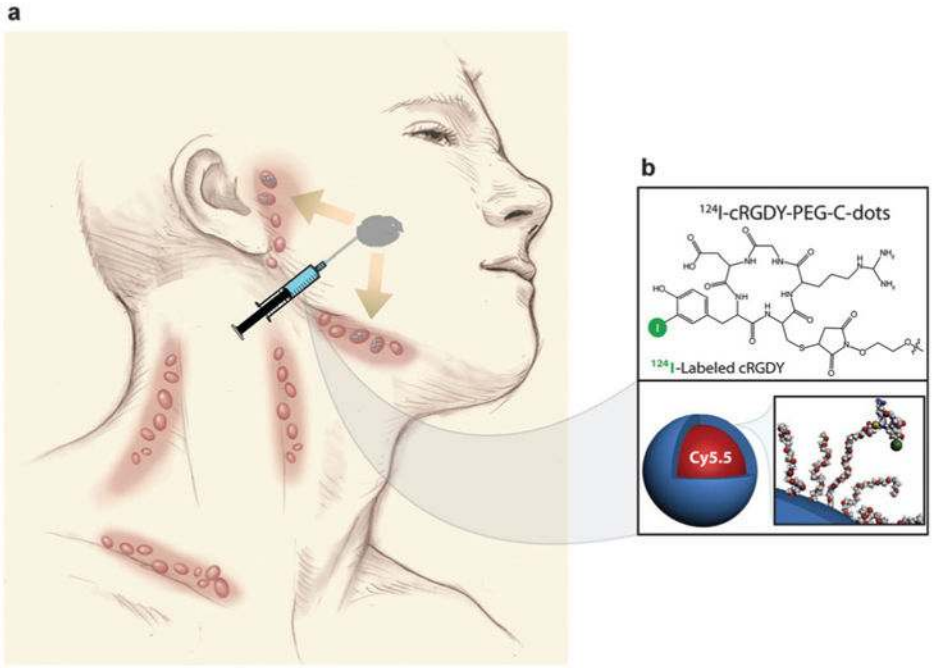

Fig. 1.

Schematic of SLN mapping in the head and neck using ^{124}I-cRGDY-PEG-C dots. (a) Injection of ^{124}I-cRGDY-PEG-C dots about an oral cavity lesion with drainage to preauricular and submandibular nodes. (b) ^{124}I-cRGDY-PEG-ylated core-shell silica nanoparticle with surface-bearing radiolabels and peptides and core-containing reactive dye molecules (insets).

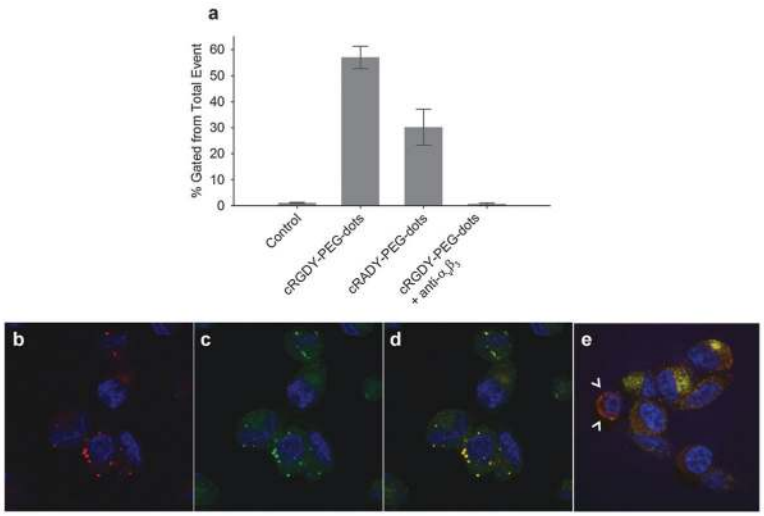

Fig. 2.

Specific binding and internalization of cRGDY-PEG-C dots in a human melanoma cell line (M21). (a) Specific binding of cRGDY-PEG-C dots to M21 cells. Binding of cRGDY-PEG-dots to M21 cells and $\alpha_v\beta_3$-integrin receptor blocking by flow cytometry using an anti-$\alpha_v\beta_3$ antibody before particle probe incubation. Non-specific binding using media alone and a scrambled peptide-bound construct, cRADY-PEG-dots (controls) is shown. (Adapted from *J. Clin. Invest.*, 2011, **121**, 2768–2780) (b–d) cRGDY-PEG-C dots colocalize with endosomal and macropinocytosis markers using confocal microscopy. (b) Uptake of cRGDY-PEG-C dots into M21 cells (red puncta) with Hoechst counterstaining (blue). (c) LysoTracker Red labeling of acidic organelles (green puncta) with Hoechst counterstaining. (d) Colocalization of cRGDY-PEG-C dots with LysoTracker Red staining (yellow puncta). (e) Colocalization of cRGDY-PEG-C dots with FITC-dextran staining (yellow areas). Surface-bound cRGDY-PEG-C dots are shown around the cell periphery (arrowheads). 63× magnification images.

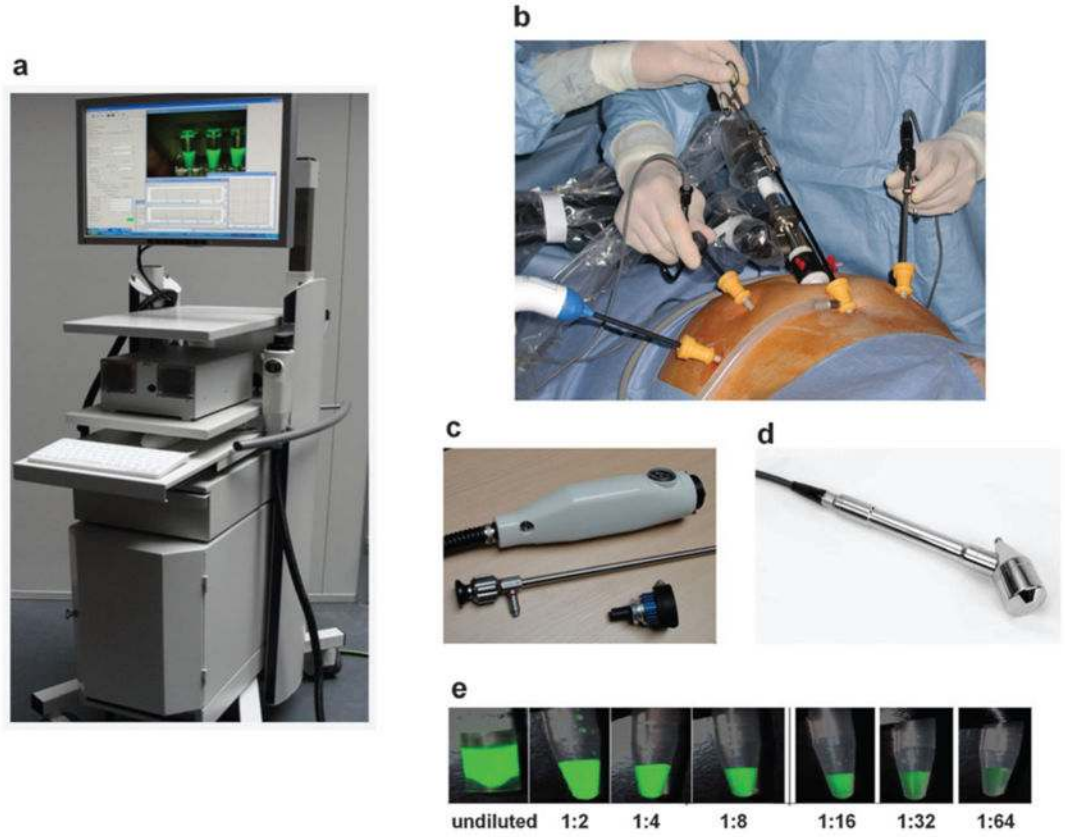

Fig. 3.

Minimally invasive surgery utilizing a handheld fluorescence camera system. (a) ArteMIS™ handheld camera fluorescence imaging system for open and laparoscopic procedures. (b) Minimally invasive surgery using laparoscopic tools. (c) System components (top to bottom): camera, laparoscope, and ring light. (d) Handheld gamma probe for radiodetection. (e) Optical imaging of a serial dilution of 10 nm Cy5.5-containing cRGDY-PEG-C dots (exposure = 60 ms; gain = 125; laser power = 85%; camera distance = 175 mm).

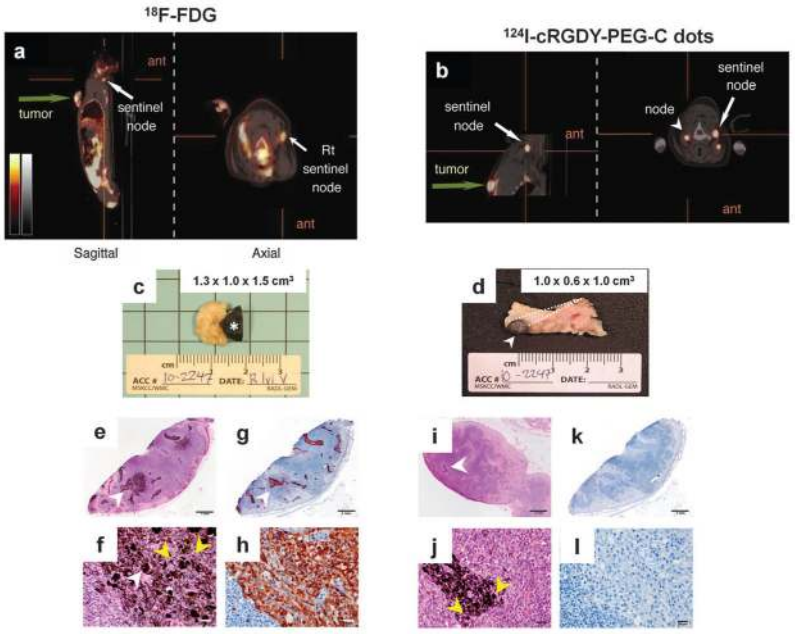

Fig. 4.

Imaging of metastatic disease in a spontaneous melanoma miniswine model. (a) Whole-body ^{18}F-FDG PET-CT sagittal and axial views demonstrating primary tumor (green arrow) and single SLN (white arrow) posteriorly within the right (Rt) neck after i.v. injection. ant, anterior. (b) High-resolution PET-CT scan reveals bilateral nodes 1 hour after subdermal, 4-quadrant, peritumoral injection of ^{124}I-cRGDY-PEG-C dots (SLN, arrow; left-sided node, arrowhead). (c, d) Gross images of the cut surfaces of the black-pigmented SLN (asterisk, c) and contralateral metastatic node (arrowhead, d) in the left posterior neck. (e) Low-power view of H&E-stained SLN demonstrating scattered melanomatous clusters (white arrowhead). (f) Corresponding high-power view of H&E-stained SLN, revealing melanoma cells (yellow arrowheads) and melanophages (white arrowhead). (g) Low-power image of a melanoma-specific marker, HMB-45 (white arrowhead), in representative SLN tissue. (h) High-power image of HMB-45-stained SLN tissue. (i) Low-power view of H&E-stained contralateral lymph node showing scattered melanomatous clusters (white arrowhead). (j) High-power image of contralateral node showing infiltration of melanomatous cells (yellow arrowheads). (k) Low-power image of representative normal porcine nodal tissue. (l) High-power image of representative normal porcine nodal tissue. Scale bars: 1 mm (e, g, i, k); 20 μm (f, h, j, l). (Adapted from *J. Clin. Invest.*, 2011, **121**, 2768–2780).

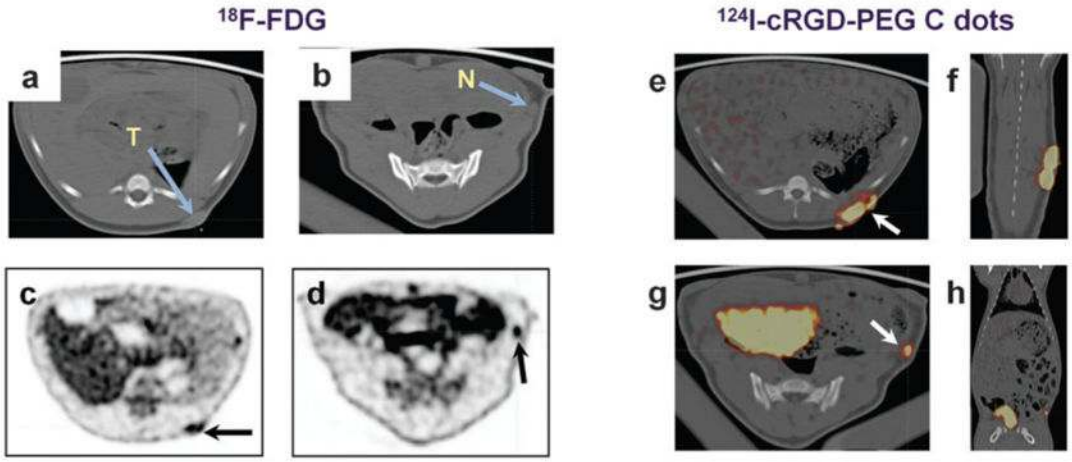

i

LOCATION	ACTIVITY (counts/sec)
Primary	2165 ± 47
SLN (in vivo)	2664 ± 52
SLN (ex vivo)	421 ± 21
Bkgd (foot)	141 ± 12

Fig. 5.

Image-guided SLN Mapping in a spontaneous melanoma miniswine model: Pre-operative PET imaging. (a, b) Axial CT images reveal a left pelvic soft tissue mass (a, blue arrow) and left flank SLN (b, blue arrow). (c, d) Axial ^{18}F-FDG PET images show localized activity within the tumor (c, black arrow) and left flank SLN (d, black arrow) following i.v. tracer injection. (e) Axial and (f) coronal ^{124}I-cRGDY-PEG-C dot co-registered PET-CT images show site of local injection about the pelvic lesion (e, white arrow). (g) Corresponding axial and (h) coronal co-registered PET-CT images localize activity to the SLN (g, white arrow). Large bladder uptake is also evident in both images. (i) Radioactivity levels of the primary tumor, SLN (*in vivo*, *ex vivo*), and a site remote from the primary tumor (*i.e.*, background), using a handheld gamma probe.

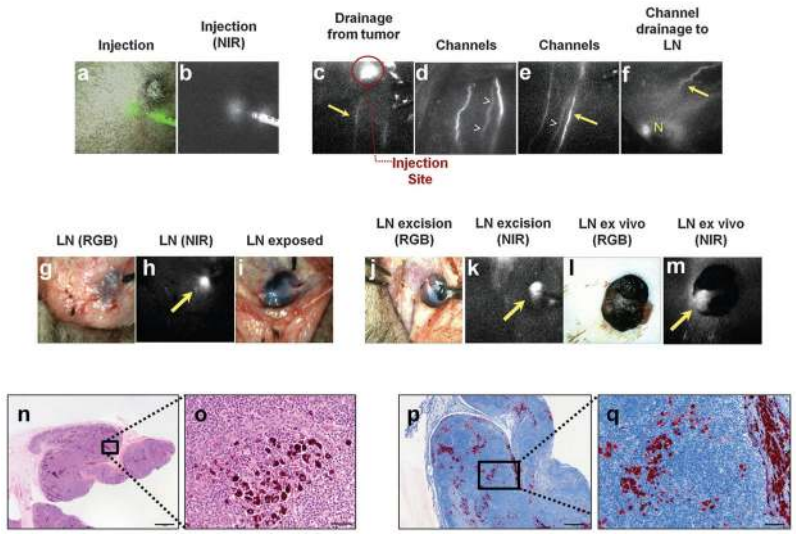

Fig. 6.

Image-guided SLN mapping in a spontaneous melanoma miniswine model: Real-time intraoperative optical imaging with correlative histology. Intraoperative SLN mapping was performed on the animal shown in Fig. 5. (a–i) Two-channel NIR optical imaging of the exposed nodal basin. Local injection of Cy5.5-incorporated particles displayed in dual-channel model (a) RGB color (green) and (b) NIR fluorescent channels (white). (c–f) Draining lymphatics distal to the site of injection. Fluorescence signal within the main draining proximal (c, d), mid (e), and distal (f) lymphatic channels (yellow arrows) extending toward the SLN ('N'). Smaller caliber channels are also shown (arrowheads). Images of the SLN displayed in the (g) color and (h) NIR channels. (i) Color image of the exposed SLN. (j–m) Images of SLN in the color and NIR channels during (j, k) and following (l, m) excision, respectively. (n) Low power view of H&E stained SLN shows cluster of pigmented cells (black box) (bar = 1 mm). (o) Higher magnification of (n) reveals rounded pigmented melanoma cells and melanophages (bar = 50 μm). (p) Low power view of HMB-45-stained (red) SLN confirms presence of metastases (black box, bar = 500 μm). (q) Higher magnification in (p) reveals clusters of HMB-45+ expressing melanoma cells (bar = 100 μm).

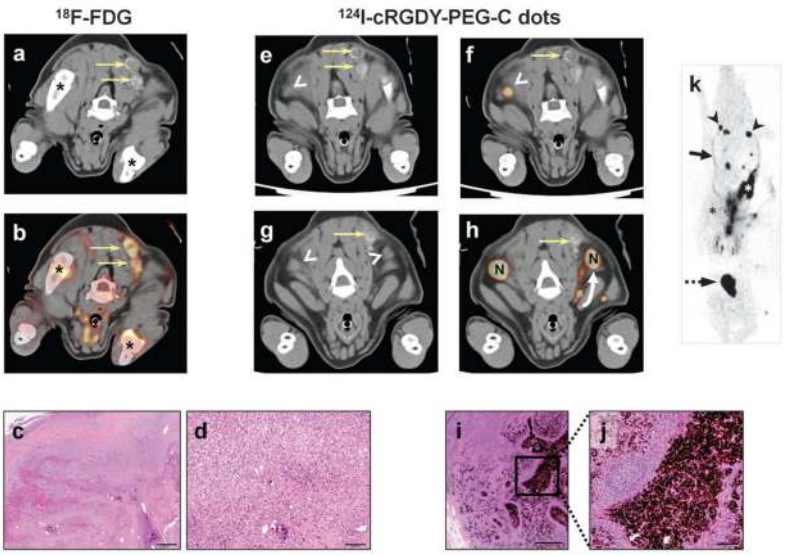

Fig. 7.

Discrimination of inflammation from metastatic disease: comparison of ^{18}F-FDG and ^{124}I-cRGDY-PEG-C dot tracers. (a–d) Imaging of inflammatory changes using ^{18}F-FDG-PET with tissue correlation. (a) Axial CT scan of the ^{18}F-FDG PET study shows calcification within the left posterior neck (yellow arrows). (b) Fused axial ^{18}F-FDG PET-CT reveals hypermetabolic activity at this same site (yellow arrows). Increased PET signal is also seen in metabolically active osseous structures (asterisks). (c) Lowand (d) high-power views of H&E-stained calcified tissue demonstrate extensive infiltration of inflammatory cells. (e–k) Metastatic disease detection following injection of ^{124}I-cRGDY-PEG C dots about the tumor site. (e) Pre-injection axial CT scan of ^{124}I-cRGDY-PEG-C dots shows calcified soft tissues within the posterior neck (yellow arrows). (f) Co-registered PET-CT shows no evident activity corresponding to calcified areas (arrow), but demonstrates a PET-avid node on the right (arrowhead). (g) Axial CT at a more superior level shows nodes (arrowheads) bilaterally and a calcified focus (yellow arrow). (h) Fused PET-CT demonstrates PET-avid nodes (N) and lymphatic drainage (curved arrow). Calcification shows no activity (arrow). (i) Low- and (j) high-power views confirm the presence of nodal metastases. (k) Single frame from a three-dimensional (3D) PET image reconstruction shows multiple bilateral metastatic nodes (arrowheads) and lymphatic channels (solid arrow) draining injection site (white asterisk). Bladder activity is seen (dashed arrow) with no significant tracer accumulation in the liver (black asterisk). Bladder activity is seen with no significant tracer accumulation in the liver. Scale bars: 500 μm (c, d); 100 μm (i, j).

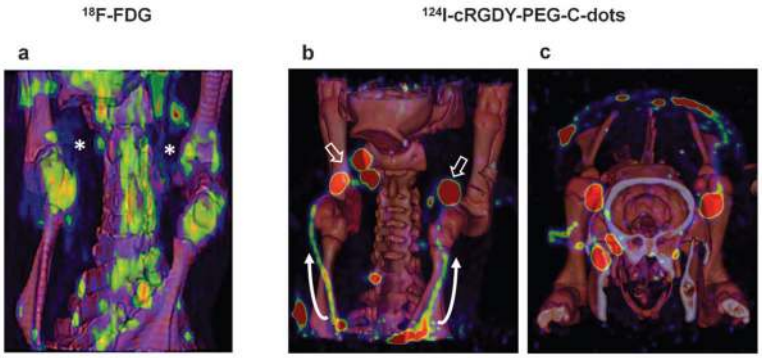

Fig. 8.

3D integrated ^{18}F-FDG and ^{124}I-cRGDY-PEG-C dot PET-CT. (a–c) 3D volume rendered images were generated from CT and PET imaging data shown in Fig. 7. (a) PET-CT fusion image (coronal view) shows no evident nodal metastases (asterisks). Increased activity within bony structures is identified. (b, c) High-resolution PET-CT fusion images showing coronal (b) and superior views (c) of bilateral metastatic nodes (open arrows) and lymphatic channels (curved arrows) within the neck following local injection of ^{124}I-cRGDY-PEG-C dots.

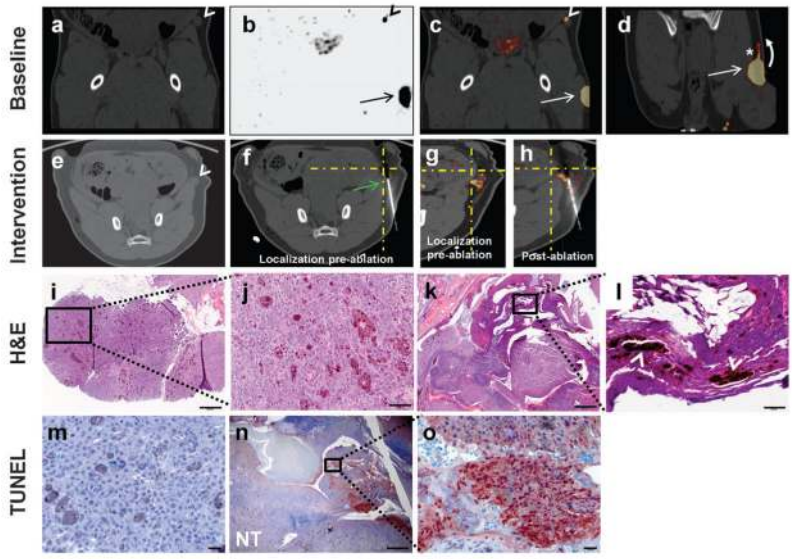

Fig. 9.

Assessment of treatment response after radiofrequency ablation (RFA) using ^{124}I-cRGDY-PEG-C dots (a–c) Single-dose ^{124}I-cRGDY-PEG-C dot localization of the SLN. (a) Baseline coronal CT (white arrowhead), (b) PET (black arrowhead), and (c) fused PET-CT images (white arrowhead) following a peritumoral injection. (b–d) Tumor ^{124}IcRGDY- PEG-C dot activity. (b) PET-avid exophytic left pelvic mass (black arrow). (c, d) Combined PET-CT images showing a PET-avid lesion (white arrow) and ^{124}I-cRGDY-PEG-C dot flow within a draining lymphatic channel (asterisk) towards the SLN (curved arrow). (e, f) Pre-ablation axial CT images locate the SLN (e, white arrowhead) prior to RFA electrode placement (f, arrow) into the node (below crosshairs). (g) Pre-ablation fused PET-CT reveals increased SLN activity (posterior to cross-hairs). (h) Postablation PET-CT scan shows mildly reduced activity at the SLN site, anterior to the needle tip. (i) Corresponding pre-ablation H&E staining of core biopsy tissue from the SLN confirms pigmented tumor infiltration (bar = 200 μm). (j) High magnification of boxed area in (i) reveals large, rounded pigmented clusters of melanoma cells (bar = 50 μm). (k) Post-ablation H&E staining shows necrotic changes within a partially tumor-infiltrated node (box) and multifocal hemorrhages (bar = 500 μm). (l) High magnification of (k) reveals significant tissue necrosis (arrowheads) within the metastatic node, in addition to lymphoid tissue (bar = 50 μm). (m) TUNEL staining of metastatic SLN before ablation (bar = 20 μm). (n) Post-ablation TUNEL staining demonstrating focal areas of necrosis (red) with adjacent scattered tumor foci and normal nodal tissue (NT) (bar = 500 μm). (o) High magnification of boxed area in (n) shows positive TUNEL staining (red area), consistent with necrosis (bar = 20 μm).